# Aircraft-to-Aircraft Channel Measurements in the VHF/UHF Band: Analysis of the Line-of-Sight and Lake-Reflected Channel Components

Miguel A. Bellido-Manganell
*German Aerospace Center (DLR)*
Muenchner Str. 20
82234 Wessling, Germany
Miguel.BellidoManganell@dlr.de
https://orcid.org/0000-0002-0668-3477

Uwe-Carsten Fiebig
*German Aerospace Center (DLR)*
Muenchner Str. 20
82234 Wessling, Germany
Uwe-Carsten.Fiebig@dlr.de
https://orcid.org/0000-0003-2736-1140

Michael Walter
*German Aerospace Center (DLR)*
Muenchner Str. 20
82234 Wessling, Germany
M.Walter@dlr.de
https://orcid.org/0000-0001-5659-8716

***Abstract*—This paper presents a statistical analysis of the main components of the aircraft-to-aircraft channel based on the wideband channel measurements conducted between two aircraft in the VHF/UHF band at 250 MHz. We consider multiple flight segments where the aircraft flew at diverse altitudes and used different antennas for transmission and for reception, alternating between a top and a bottom antenna. In each scenario of interest, we analyse the power and the small-scale fading of the envelope of the direct line-of-sight component and of the specular reflection component off a lake. For both components, we compare the measured average power with the theoretical free-space path loss, and the measured small-scale fading with multiple well-known statistical distributions. The results show that the envelope of both components is strongly affected by the geometry, the location of the antennas, and by the aircraft fuselage itself. The different scenarios yield significant variations in the average power and in the distribution of the small-scale fading. A Rician distribution shows the best fit for the line-of-sight component envelope. The component reflected off the lake can be modeled by a Rician distribution when it is not obstructed or strongly affected by the aircraft fuselage, and by a Nakagami distribution otherwise. The parameters of the best-fitting distributions, including the Rician $K$-factor, are provided for the different scenarios.**

***Index Terms*—Air-to-air, aircraft-to-aircraft (A2A), wireless channel, aircraft, antenna, ground reflection, Rician, Nakagami.**

## I. Introduction

Air-to-air communications have gained significant attention over the last decades with the development of communication and surveillance systems for aircraft, drones, and other flying vehicles. These systems, based on low-latency, high-throughput air-to-air (A2A) data links, will allow the vehicles to detect and avoid collisions, to operate without air traffic control support, and to establish ad hoc networks to exchange, relay, and disseminate information. Some of these A2A communication systems are already being developed, e.g., for aircraft [1]. Nonetheless, in order to achieve an optimal design, knowledge of the A2A channel is required. Such knowledge can be gained through channel measurements, which become very expensive and challenging for vehicles like aircraft. This leads to the scarcity of measurement-based wideband A2A channel models seen in the literature, especially for aircraft.

This paper aims at providing useful information about the A2A channel that can be used for the development of realistic channel models and for the design of advanced A2A data links. We present a statistical analysis of the main components of the A2A channel based on wideband channel measurements conducted between two aircraft in the VHF/UHF band at 250 MHz [2]. A previous analysis of these components was limited to a single antenna configuration and a single aircraft altitude [3]. In our work, we consider multiple flight segments where the aircraft flew at diverse altitudes and used different antennas for transmission and for reception, alternating between a top and a bottom antenna. In each scenario of interest, we analyse statistically the power and the small-scale fluctuations of the main components of the channel: the direct line-of-sight (LOS) component and the specular reflection (SR) component off a lake. For both components, we compare the measured average power with the theoretical free-space path loss (FSPL), and the measured small-scale fading with multiple well-known statistical distributions. The results show that, in all considered scenarios, both components are strongly affected by the geometry, the location of the antennas on the aircraft, and by the aircraft fuselage itself, as they lead to significant fluctuations in the average power and fast fading. In general, the Rician distribution provides a very good fit for the LOS component envelope. The SR component can also be modeled accurately by a Rician distribution when it is not obstructed or strongly affected by parts of the fuselage. In such cases, however, the Nakagami distribution shows a significantly better fit. The parameters of the best-fitting distributions, including the Rician $K$-factor, are provided for the different scenarios.

This paper is structured as follows. We describe the aircraft-to-aircraft channel measurements in Section II, which is followed by the definition of the scenarios of interest in Section III and by a description of the applied methodology in Section IV. We show and discuss the results of our analysis in Section V and draw our conclusions in Section VI.


(a) Cessna aircraft (transmitter)


(b) Dornier aircraft (receiver)

Fig. 1. Airplanes and antenna positions. The transmitter was located in the Cessna (Fig. 1a) and the receiver in the Dornier (Fig. 1b). The Cessna flew behind the Dornier. The propagation channel has been tested for four antenna configurations, i.e. "down-to-down", "down-to-up", "up-to-down", and "up-to-up", where "down" denotes the bottom antenna and "up" denotes the top antenna. The antennas at the Cessna were located approximately in the middle of its fuselage, right behind its wings. The Dornier had the top antenna mounted between the wings and the cockpit, i.e., between both propellers, and the bottom antenna close to its tail.

TABLE I
PARAMETERS OF THE A2A CHANNEL MEASUREMENTS [2]

| | |
|---|---|
| Carrier frequency | 250 MHz |
| Bandwidth | 20 MHz |
| Measurement time grid | 2.048 ms |
| Signal period | 25.6 µs |
| Delay resolution | 50 ns |
| Max. Doppler frequency | ±244 Hz |
| Airborne antennas | UHF blade antennas (*Cooper 21-30-18*) |
| Polarization | vertical |
| Transmit power | 42.15 dBm EIRP |

TABLE II
SCENARIOS FOR THE LOS COMPONENT (AGL = ABOVE GROUND LEVEL)

| Scenario identifier | Antenna configuration TX → RX | TX height AGL (m) | RX height AGL (m) |
|---|---|---|---|
| LOS-D-D-600-600 | down → down | 600 | 600 |
| LOS-D-D-1600-1600 | down → down | 1600 | 1600 |
| LOS-D-D-2600-2600 | down → down | 2600 | 2600 |
| LOS-D-U-600-600 | down → up | 600 | 600 |
| LOS-U-D-600-600 | up → down | 600 | 600 |
| LOS-U-U-600-600 | up → up | 600 | 600 |
| LOS-D-D-1600-600 | down → down | 1600 | 600 |
| LOS-D-U-1600-600 | down → up | 1600 | 600 |
| LOS-U-D-1600-600 | up → down | 1600 | 600 |
| LOS-U-U-1600-600 | up → up | 1600 | 600 |

## II. AIRCRAFT-TO-AIRCRAFT CHANNEL MEASUREMENTS

The aircraft-to-aircraft channel measurement campaign [2] was conducted in 2009 in southern Germany using the Cessna Grand Caravan C-208B (D-FDLR) and the Dornier Do-228-101 (D-CODE) airplanes shown in Fig. 1. A Medav RUSK channel sounder [4] was employed. The Cessna aircraft carrying the transmitter flew behind the Dornier aircraft carrying the receiver. The channel was measured using one antenna for transmission and one for reception, i.e., a SISO configuration. As shown in Fig. 1, each aircraft had a top antenna facing upwards ("U" antenna) and a bottom antenna facing downwards ("D" antenna). Thus, multiple flights were conducted alternating between both antennas, both for transmission and for reception, and the channel was measured using all four possible antenna configurations. The antennas at the Cessna were located approximately in the middle of its fuselage, right behind its wings, whereas the Dornier had the top antenna mounted between the wings and the cockpit, practically between both propellers, and the bottom antenna close to its tail. The main parameters of the channel measurements are shown in Table I. The channel, or more accurately its transfer function (TF), was measured using a carrier frequency of 250 MHz every 2.048 ms with a bandwidth of 20 MHz and achieving, consequently, a delay resolution of 50 ns. For simplicity, we refer hereinafter to the Cessna as the transmitter (TX) and to the Dornier as the receiver (RX).

## III. SCENARIOS OF INTEREST

We use the channel measurements to describe statistically the LOS and SR components of the channel. However, we do not analyse all measurements jointly, but split the flights into multiple scenarios of interest where the different configurations are tested, such as different antenna configurations and aircraft altitudes. We additionally distinguish between the scenarios used to analyse the LOS and SR components, given that the latter is only evaluated when the aircraft fly over a lake, i.e., when the specular reflection is caused by a lake. The scenarios considered for the LOS and SR components are described in Table II and Table III, respectively. In each scenario, both aircraft tried to maintain a constant altitude and distance between them. However, the aircraft had to do short-term flight track corrections, which were in general unavoidable and can be expected in a normal flight. The considered scenarios allow us to isolate the impact that either the antenna position or the altitudes of the airplanes had on the LOS and SR components, as the same antenna configuration was used at multiple altitudes, and different antenna configurations were tested at the same altitude. Note that the scenario identifier is given such that it is easy to identify its parameters, e.g., LOS-U-D-1600-600 means that the scenario is used to analyse the LOS component, that TX uses the top antenna facing upwards ("U") and RX uses the bottom antenna facing downwards ("D"), and that TX and RX fly at 1600 m and 600 m above ground level, respectively. Fig. 2 shows the flight tracks.

It is to be noticed that we only consider the flight segments with no significant flight maneuvers, such as banking turns or steep changes in the aircraft altitude. This is due to the

TABLE III
SCENARIOS FOR THE SR COMPONENT (AGL = ABOVE GROUND LEVEL)

| Scenario identifier | Antenna configuration TX → RX | TX height AGL (m) | RX height AGL (m) |
|---|---|---|---|
| SR-D-D-600-600 | down → down | 600 | 600 |
| SR-D-D-1600-1600 | down → down | 1600 | 1600 |
| SR-D-U-600-600 | down → up | 600 | 600 |
| SR-U-D-600-600 | up → down | 600 | 600 |
| SR-U-U-600-600 | up → up | 600 | 600 |

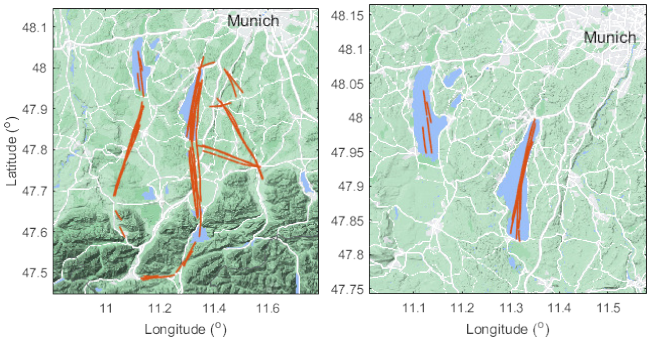


(a) Tracks flown to measure the LOS component

(b) Tracks flown to measure the lake-reflected SR component

Fig. 2. TX tracks flown for the measurement of the LOS and SR components. Copyright of map: Map data ©2021 GeoBasis-DE/BKG (©2009), Google.

significant signal power loss observed during such maneuvers, which makes the analysis extremely complex and too dependent on the specific maneuver and its duration. As an example, we show in Fig. 3 the flight track during a segment of the flight and the measured LOS component power relative to the theoretical FSPL. We can see that the LOS component power decreases significantly, in some cases over 15 dB, when the airplanes conduct banking turns, and stays stable otherwise.

## IV. METHODOLOGY

The TF of the channel, $T(m,n)$, is measured every $2.048\,\text{ms}$, with $m$ being the time index and $n = 0, 1, ..., N-1$,

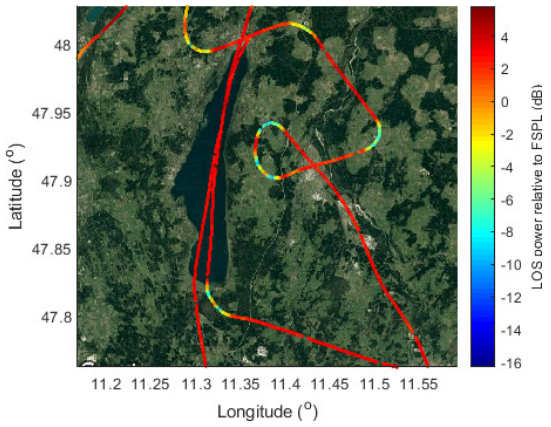


Fig. 3. Example of the effect of banking maneuvers on the LOS component power relative to the theoretical FSPL. The signal power decreases significantly during banking turns. Copyright of map: Map data ©2021 GeoBasis-DE/BKG (©2009), Google.

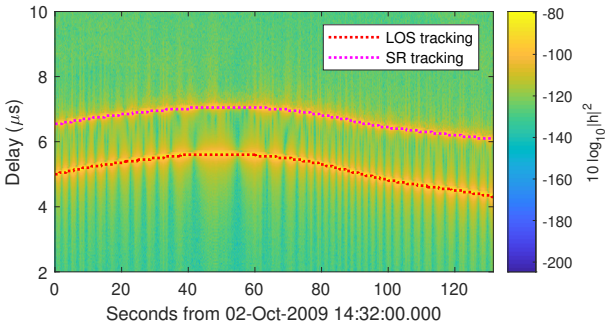


Fig. 4. Time-variant PDP measured in one of the flight segments. Only a delay up to $10\,\mu\text{s}$ is shown here for simplicity, although the CIR is measured for a delay up to $25.6\,\mu\text{s}$. The tracking of the LOS and SR components is shown on the PDP. The delay of both components is accurately estimated for each measured CIR.

with $N = 513$, the frequency bin index. The channel impulse response (CIR) of the channel can then be obtained as

$$h(m,k) = \frac{1}{N}\sum_{n} T(m,n) e^{\mathrm{j}\frac{2\pi}{N}nk}, \tag{1}$$

where $k = 0, 1, ..., N-1$ denotes the delay bin index. As an example, Fig. 4 shows the time-variant power delay profile (PDP) built using the CIRs measured in one of the flight segments.

### A. Tracking the LOS and SR components

In order to calculate the power of the LOS and SR components separately for each measured CIR, we must first estimate the delay bin where each component is received. For this, we develop a simple algorithm to track the LOS and SR components. Our algorithm is capable of detecting the LOS and SR components given that, in all considered scenarios, both components are sufficiently separated from each other in delay and present a power significantly higher than other multi-path components (MPCs), being also the LOS component generally stronger than the SR component. In addition, although both components present short-term fluctuations in power, which are specially abrupt for the SR component, one can exploit their long-term power stability in the considered scenarios to track them first for a block of consecutive CIRs, and then to accurately estimate their delays for each CIR separately. As shown in Fig. 4 for one of the flight segments considered in our analysis, our algorithm is capable of correctly tracking the LOS and SR components for each measured CIR in all the scenarios. Given that it is not the focus of this work, and that we only validated our algorithm in the analysed scenarios, where the above-mentioned assumptions apply, we do not describe the tracking algorithm here.

### B. Measuring the power of the LOS and SR components

We now measure the power of the LOS and SR components separately for each CIR. Given that the channel measurements are conducted with a finite bandwidth, it can be shown from (1) that the components do not appear in a single delay bin but spread among consecutive delay bins following a

$f_{\mathrm{s}}(k) = \mathrm{sinc}\left(k - B\tau\right) / \mathrm{sinc}\left(\frac{1}{N}\left(k - B\tau\right)\right)$ pattern, where $\tau$ is the delay of the component and $B = 20$ MHz in our case. This can be observed in the LOS component in Fig. 4, whose width varies in delay as the aircraft move and $f_{\mathrm{s}}(k)$ becomes wider or narrower depending on the difference between the actual LOS component delay and the sampling instant. Based on this, we compute the power of each component by applying a window in delay around the central delay of each component, estimated as shown in Fig. 4, such that

$$P(m) = \sum_{n'=n_{\mathrm{c}}-\frac{N_{\mathrm{w}}-1}{2}}^{n_{\mathrm{c}}+\frac{N_{\mathrm{w}}-1}{2}} |h(m,n')|^2 \,, \tag{2}$$

where $n_{\mathrm{c}}$ is the delay bin where the component was detected by the tracking algorithm, and $N_{\mathrm{w}}$ is the number of delay bins of the delay window. Using (2), we can obtain the power of the LOS and SR components as $P_{\mathrm{los}}$ and $P_{\mathrm{sr}}$, respectively, using the different $n_{\mathrm{c}}$ estimated for each component by the tracking algorithm. Of course, the number of delay bins $N_{\mathrm{w}}$ must be high enough to accurately measure each component, while it should not be too high as other components might also be wrongly included in the power measurement. In practice, increasing $N_{\mathrm{w}}$ reduces the delay resolution of the measurements. We use $N_{\mathrm{w}} = 5$, or equivalently $250\,\mathrm{ns}$, which yields an accurate measurement of the power of the LOS and SR components and still entails a high delay resolution.

We can now compare the received power of each component, i.e, $P_{\mathrm{los}}$ and $P_{\mathrm{sr}}$, with the power expected in theory if only the FSPL between TX and RX is taken into account, which can be obtained as

$$L_{\mathrm{pl}}(m) = \left(\frac{c}{4\pi f_{\mathrm{c}} d(m)}\right)^2 , \tag{3}$$

where $f_{\mathrm{c}} = 250$ MHz, $c$ is the speed of light and $d(m)$ is the distance travelled by the component at the time index $m$, i.e., $d_{\mathrm{los}}(m)$ and $d_{\mathrm{sr}}(m)$ for the LOS and SR components, respectively. These distances can be derived from the delay estimated by the tracking algorithm for each component.

Logically, $P$ is also affected by the transmitting and receiving antenna gains, which change with the geometry between TX and RX, as well as the ground in the case of the SR component. Unfortunately, the exact radiation pattern of the antennas mounted on the aircraft is not know. However, according to the manufacturer, the antennas are omnidirectional in the azimuth plane and present a maximum gain of 4 dBi. From lab measurements conducted by the manufacturer, the main radiation lobe spans approximately elevations from 5 to 40 degrees, decreasing rapidly for higher elevation angles.

### C. Computing the small-scale fading

In order to characterize the small-scale fading of each component, we first remove the large-scale fading from the measurements by applying a moving average filter as in [5]. Thus, we have to assume the channel to be stationary during the filter length of $M_{\mathrm{w}}$ samples. We choose $M_{\mathrm{w}}$ such that a distance of $70\lambda$ is covered by the aircraft. Thus, $M_{\mathrm{w}}$ changes according to the slowly-changing average aircraft speed in each flight segment. Similar analyses consider higher distances with respect to the signal wavelength, i.e., over $100\lambda$ in [5] and $170\lambda$ in [6]. Thus, we obtain the large-scale power of each component as

$$P_{\mathrm{LS}}(m) = \frac{1}{M_{\mathrm{w}}} \sum_{m'=m-M_{\mathrm{w}}/2}^{m+M_{\mathrm{w}}/2-1} P(m') \tag{4}$$

and the amplitude of each component without large-scale fading as

$$|h'(m)| = \sqrt{\frac{P(m)}{P_{\mathrm{LS}}(m)}} \,. \tag{5}$$

Note that we obtain the power $P_{\mathrm{LS}}$ as an average of the component under test, i.e., either the LOS or the SR component, whereas other works, such as [5], use an average of all channel components. We opt for this normalization as we want to analyse each component independently from the others.

We compare the envelope distribution of the LOS and SR components with multiple fading distributions commonly considered in the literature. We base our comparison on the Kolmogorov–Smirnov (KS) test as a goodness-of-fit (GoF) indicator [7], which is obtained as

$$\mathrm{GoF} = \sup_z |F_Z(z) - F_0(z)| \,, \tag{6}$$

where sup is the supremum, $F_Z(z)$ is the cumulative distribution function (CDF) of the measured data, and $F_0(z)$ is the CDF of the fitted distribution.

The Rician distribution is one of the most common distributions to model the small-scale fading and, as shown in Section V, yields a good fit for the fading observed in many scenarios. Its probability density function (PDF) is given by

$$f_{\mathrm{ric}}(x) = 2\tfrac{(K+1)x}{\Omega} e^{-\left(K+\frac{(K+1)x^2}{\Omega}\right)} \mathrm{I}_0\left(2\sqrt{\tfrac{K(K+1)}{\Omega}}x\right) , \tag{7}$$

where $K$ is known as the Rician $K$-factor and represents the power ratio of the dominant path to the MPCs causing the fast fading, $\Omega = \mathrm{E}\{x^2\}$ is the average power with $\mathrm{E}\{\cdot\}$ denoting the expectation operator, and $\mathrm{I}_0(\cdot)$ is the zero-order modified Bessel function of the first kind. We obtain the $K$-factor using the method of moments [8], [9] as

$$K = \frac{\sqrt{1-\gamma}}{1-\sqrt{1-\gamma}} \,, \tag{8}$$

where $\gamma = \frac{\mathrm{Var}\{x^2\}}{(\mathrm{E}\{x^2\})^2}$ with $\mathrm{Var}\{\cdot\}$ denoting the variance operator.

The Nakagami distribution also shows promising results for the SR component in some scenarios. Its PDF is given by

$$f_{\mathrm{nak}}(x) = 2\left(\frac{\mu}{\omega}\right)^{\mu} \frac{1}{\Gamma(\mu)} x^{(2\mu-1)} e^{-\frac{\mu}{\omega}x^2} \,, \tag{9}$$

where $\mu \geq 1/2$ is the shape parameter and $\omega > 0$ models the spread.

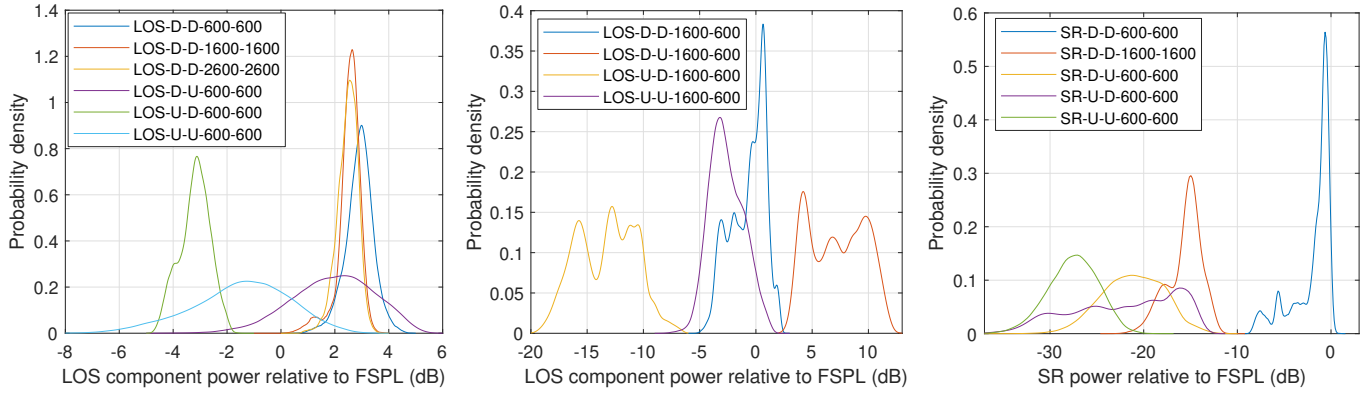


(a) LOS component (same altitude) (b) LOS component (different altitudes) (c) SR component over a lake

Fig. 5. PDF of the power of the LOS and SR components relative to the FSPL in the different scenarios of interest.

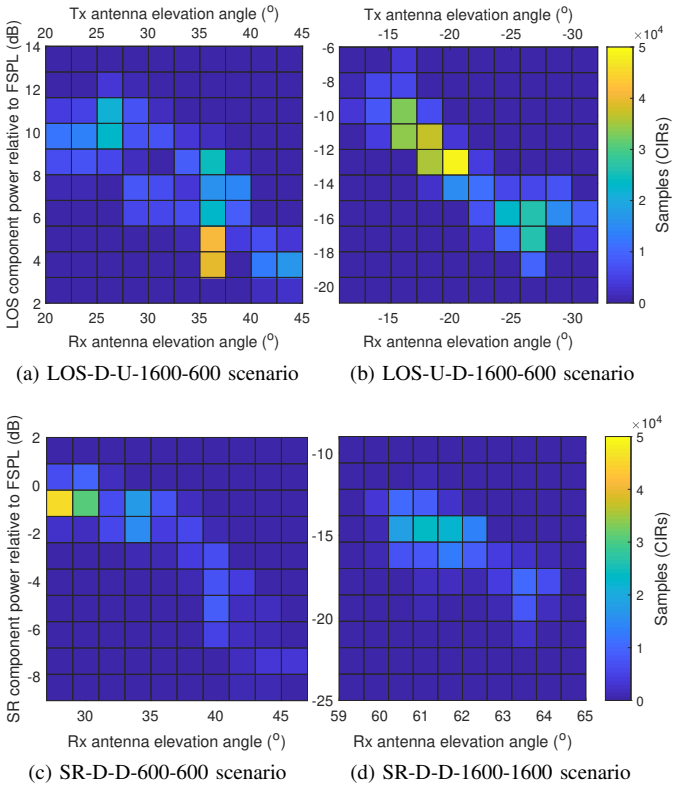


(a) LOS-D-U-1600-600 scenario (b) LOS-U-D-1600-600 scenario

(c) SR-D-D-600-600 scenario (d) SR-D-D-1600-1600 scenario

Fig. 6. Histogram of the power of the LOS (Fig. 6a and Fig. 6b) and SR (Fig. 6c and Fig. 6d) components relative to the FSPL for different TX and RX antenna elevation angles in four scenarios of interest. In Fig. 6a and Fig. 6c, one can see that the power of the LOS and SR components decreases significantly as the antenna elevation angle increases. The negative angles in Fig. 6b indicate non-LOS conditions between both antennas. A lower negative angle leads to more aircraft fuselage blocking and attenuating the signal. Note that the horizontal axes have been reversed for negative angles.

## V. Results

### A. Power of the LOS and SR components relative to the FSPL

Fig. 5 shows the measured PDF of the power of the LOS and SR components relative to the theoretical FSPL in the different scenarios.

*1) LOS component for multiple antenna configurations with TX and RX at the same altitude:* Lets first analyse the results shown in Fig. 5a. When both aircraft fly at the same altitude and the bottom antennas are employed, the LOS component presents a stable relative power concentrated between 2 dB and 4 dB at all considered flight levels. This is understandable given that, in the down-to-down case, nothing obstructs the direct path between the antennas, and the elevation angle of the antennas is low, yielding a positive joint antenna gain ($> 0$ dBi). When different antenna configurations are employed, the results change significantly. Using a up-to-down antenna configuration (LOS-U-D-600-600 in Fig. 5a) yields a significantly lower power. This may be caused by the fact that the aircraft did not fly parallel to the ground but raising their noses slightly, i.e., 3.7° on average as recorded at TX in this scenario. Thus, a part of the Cessna fuselage, mainly its cockpit, obstructs the LOS path and leads to a higher attenuation compared to the other scenarios. Using the top antenna for reception (LOS-D-U-600-600 and LOS-U-U-600-600 in Fig. 5a) yields larger variations in the LOS component power, which now spans a relative power range from -6 dB up to 5 dB. Because of the aircraft pitch-up, the down-to-up configuration leads to a higher average power compared to the up-to-up case, whereas the width of their PDFs is similar. We believe that the PDF of the LOS component power is wider when the top antenna is used for reception because of the Dornier aircraft itself. First, the tail of the Dornier is located in the direct path to the top antenna (see Fig. 1b) and affects it. Second, the center wing section might also affect the signal propagation, as it is located directly behind the top antenna and is slightly elevated above the aircraft fuselage, partly blocking the LOS path. Third, the aircraft propellers are very close to the top antenna and might lead to strong rapidly-changing fluctuations of the LOS component.

*2) LOS component for multiple antenna configurations with TX and RX at different altitudes:* Fig. 5b shows the results for the four antenna configurations when TX and RX flew at $1600\,\mathrm{m}$ and $600\,\mathrm{m}$, respectively. One can see that the power varies now significantly compared to the case when the aircraft

fly at the same altitude. The highest relative power is now achieved with the down-to-up antenna configuration, which could be expected because of the geometry, i.e., LOS clearance and antenna gains maximized. The opposite case is observed in the up-to-down antenna configuration, where the direct LOS path is obstructed by both aircraft. The down-to-down and up-to-up configurations yield a more moderate LOS component power, but still covering a higher power range compared to those shown in Fig. 5a. The wider PDFs shown in Fig. 5b are partially caused by the presence of multiple peaks in the PDFs. This can be explained by the fact that the angle between both aircraft changed during each scenario, which led to fluctuations in the antenna gain and, thus, to multiple peaks in the power PDF of each scenario. We verified this by obtaining the elevation angle of the TX and RX antennas in each scenario and by depicting them together with the relative component power in a histogram, as shown for some interesting scenarios in Fig. 6. Fig. 6a shows that multiple antenna elevation angles were experienced in the LOS-D-U-1600-600 scenario and that the relative power decreased as the antenna elevation angle increased, as expected from the antenna radiation pattern. In Fig. 6b, we show the results for the LOS-U-D-1600-600 scenario. In this case, the antenna elevation angles are depicted negative in order to indicate that the antennas were located in the opposite side of the aircraft, and thus the LOS path was blocked by the aircraft fuselage. A lower negative angle represents a more obstructed LOS path, which leads to a lower relative power as shown in Fig. 6b.

*3) SR component:* Fig. 5c depicts the PDF of the SR component power relative to the FSPL for multiple antenna configurations when both aircraft flew at the same altitude. We can see a very strong and stable SR component when the bottom antennas are used at a low altitude, i.e., $600\,\mathrm{m}$. However, when the bottom antennas are used at a higher altitude, i.e., $1600\,\mathrm{m}$, the SR component power decreases significantly. This is explained by the results shown in Fig. 6c and Fig. 6d, where one can see that the SR component power at $600\,\mathrm{m}$ decreases as the antenna elevation angle increases and leaves the main antenna radiation lobe. At $1600\,\mathrm{m}$, the antenna elevation angle was much higher, i.e., between 60 and 65 degrees, which led to lower antenna gains and, consequently, to the lower SR component power shown in Fig. 5c. Of course, the reflection coefficient of the lake water also changes with the geometry and might have led to additional variations in the SR component power. In the other scenarios, the SR component is mostly blocked by the aircraft fuselage, which leads to a low power compared to the FSPL. This can be especially observed in the up-to-up antenna configuration, where the SR component power is attenuated the most.

### *B. Small-scale fading*

We now analyse the small-scale fading of the LOS and SR components measured in the scenarios of interest. The amplitude without large-scale fading, obtained using (5), is used to obtain the best fit of multiple distributions for each scenario under test. Fig. 7 shows the GoF indicator obtained

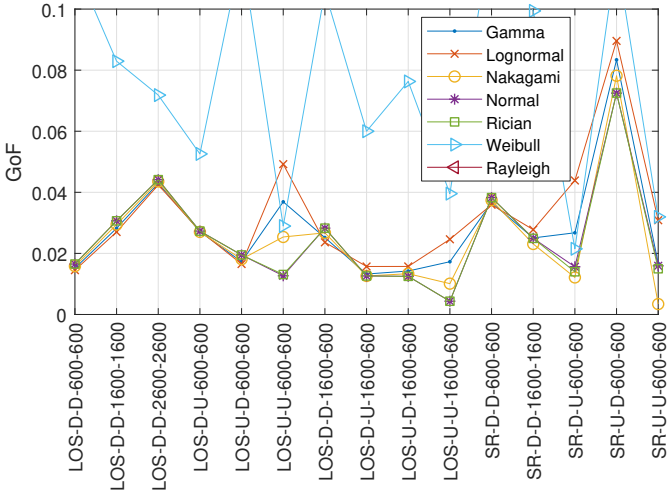


Fig. 7. Small-scale fading analysis. GoF values for different fitted distributions in the scenarios of interest for the LOS and SR components. The Rayleigh distribution provides the worst fit and its GoF falls above the depicted limits.

using (6) for the considered distributions in the scenarios of interest. With the exception of the Weibull and the Rayleigh distributions, all considered distributions are capable of achieving a good fit for the LOS component envelope, and yield similar GoF values. However, when the up-to-up antenna configuration is used, the Rician and normal distributions provide a significantly better fit than the others. The envelope of the SR component could also be realistically modeled using a Rician distribution in most scenarios. However, we can see that the Nakagami distribution achieves a better fit in some of the considered scenarios. In general, a strong SR component is well represented by a Rician distribution, e.g. in the down-to-down configuration at low altitude, and a weak SR component is well represented by a Nakagami distribution, e.g., in the up-to-up configuration. It is to be noted that no good fit is found in the SR-U-D-600-600 scenario. We believe this to be caused by short-term flight maneuvers not sufficiently compensated when removing the large-scale fading.

We show in Fig. 8 the CDF of the estimated Rician $K$-factor obtained in the different scenarios. As expected, the LOS and SR components are well represented by a high $K$-factor when the components are received with a high power, i.e., when they fall within the main antenna radiation lobe and are not obstructed by other parts of the aircraft. Another factor of importance is that the antenna is not surrounded by other objects leading to close MPCs. For example, we could see in Fig. 5b that the highest power overall was reached in the LOS-D-U-1600-600 scenario. However, the $K$-factor in this scenario is not as high as in others. As discussed before, this is caused by the use of the top antenna of the Dornier, which was affected by different parts of its fuselage, such as the tail, the propellers, and the elevated center wing section, yielding deeper variations in the signal power. In fact, one can see that the lowest $K$-factors for the LOS component are obtained

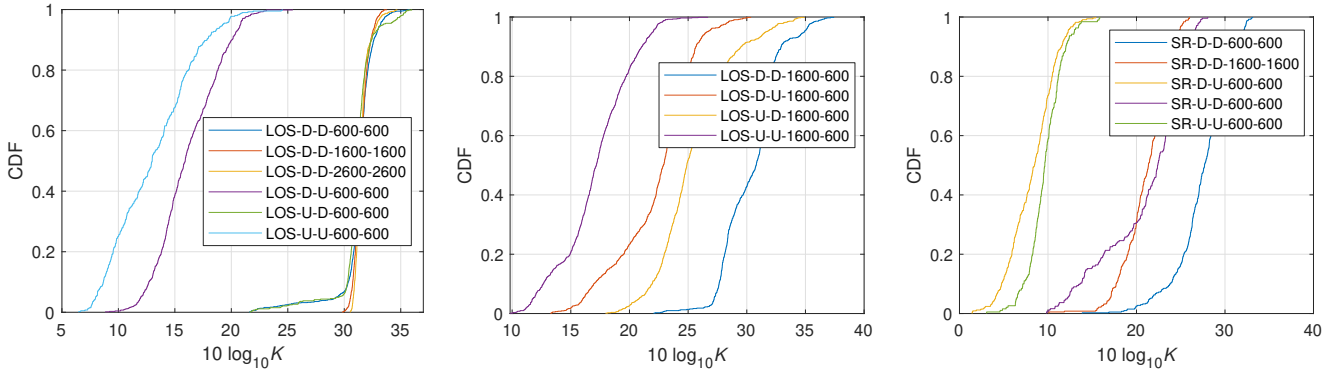


(a) LOS component at same altitude (b) LOS component at different altitude (c) SR component over lake at same altitude

Fig. 8. CDF of the estimated Rician $K$-factor in each scenario with TX and RX at the same altitude (Fig. 8a and Fig. 8c) and at different altitudes (Fig. 8b).

TABLE IV
PARAMETERS OF THE NAKAGAMI DISTRIBUTION FITTED TO THE SR COMPONENT ENVELOPE

| Scenario | $\hat{\mu}$ | Var$\{\mu\}$ | $\hat{\omega}$ | Var$\{\omega\}$ | GoF |
|---|---|---|---|---|---|
| SR-D-D-600-600 | 209.24 | 0.39 | 1.000 | 2e-8 | 0.037 |
| SR-D-D-1600-1600 | 54.15 | 0.03 | 1.000 | 9e-8 | 0.023 |
| SR-D-U-600-600 | 3.55 | 1e-4 | 0.993 | 1.5e-6 | 0.012 |
| SR-U-D-600-600 | 31.92 | 1.5e-2 | 0.997 | 2.4e-7 | 0.078 |
| SR-U-U-600-600 | 5.07 | 4.7e-4 | 0.995 | 1.9e-6 | 0.003 |

when the top antenna of the Dornier is used. A similar effect is observed for the SR component. A high $K$-factor is achieved when the SR component is not blocked by the fuselage of the aircraft, i.e., in the down-to-down antenna configuration, and a much lower $K$-factor otherwise. In the latter case, we have seen in Fig. 7 that a Nakagami distribution yields a better fit. Thus, we show in Table IV the parameters of the Nakagami distribution fitted to the envelope of the SR component in each scenario of interest. One can see that the best fit is achieved for a low variance of the $\mu$ parameter of the distribution, which happens in the scenarios using the top antenna for reception as discussed before.

## VI. CONCLUSION

This paper presents a statistical analysis of the main components of the A2A channel based on wideband channel measurements conducted between two aircraft in the VHF/UHF band at 250 MHz. We considered multiple flight segments where the aircraft flew at diverse altitudes and used different antennas for transmission and for reception, alternating between a top and a bottom antenna. We analysed the power and the small-scale fluctuations of the envelope of the LOS component and the SR component off a lake. For both components, we compared the measured average power with the theoretical FSPL, and the measured small-scale fading with multiple well-known statistical distributions. The results show that, in all considered scenarios, both components are strongly affected by the geometry, the location of the antennas on the aircraft, and by the aircraft fuselage itself, as they lead to significant fluctuations in the average power and fast fading. In general, the Rician distribution provides a very good fit for the LOS component envelope. The SR component can also be modeled accurately by a Rician distribution when it is not obstructed or strongly affected by parts of the fuselage. In such cases, however, the Nakagami distribution provides a significantly better fit.

## ACKNOWLEDGMENT

This work was partly co-funded under the research program LuFo V-3 ("Luftfahrtforschungsprogramm") of the German Federal Ministry of Economy and Energy (BMWi). The authors wish to thank all colleagues involved in the channel measurement campaign. Special thanks go to Rohde & Schwarz GmbH & Co. KG. for providing the A2A measurement data.

## REFERENCES

[1] M. A. Bellido-Manganell and M. Schnell, "Towards modern air-to-air communications: the LDACS A2A mode," in *Proc. IEEE/AIAA 38th Digital Avionics Systems Conf. (DASC)*, San Diego, CA, USA, Sep. 2019, pp. 1–10.

[2] M. Walter, S. Gligorević, T. Detert, and M. Schnell, "UHF/VHF air-to-air propagation measurements," in *Proc. 4th Eur. Conf. on Antennas and Propag. (EuCAP)*, Barcelona, Spain, Apr. 2010, pp. 1–5.

[3] M. Walter and M. Schnell, "Statistical distribution of line-of-sight and reflected path in the aeronautical channel," in *Proc. IEEE/AIAA 30th Digital Avionics Syst. Conf. (DASC)*, Seattle, WA, USA, Oct. 2011, pp. 4D1–1–4D1–9.

[4] P. Unterhuber, S. Pfletschinger, S. Sand, M. Soliman, T. Jost, A. Arriola, I. Val, C. Cruces, J. Moreno, J. P. García-Nieto *et al.*, "A survey of channel measurements and models for current and future railway communication systems," *Mobile Information Systems*, vol. 2016, 2016.

[5] L. Bernadó, T. Zemen, F. Tufvesson, A. F. Molisch, and C. F. Mecklenbräuker, "Time-and frequency-varying $K$-factor of non-stationary vehicular channels for safety-relevant scenarios," *IEEE Transactions on Intelligent Transportation Systems*, vol. 16, no. 2, pp. 1007–1017, 2014.

[6] W. Wang, R. Raulefs, and T. Jost, "Fading characteristics of maritime propagation channel for beyond geometrical horizon communications in C-band," *CEAS Space Journal*, vol. 11, no. 1, pp. 95–104, 2019.

[7] F. J. Massey Jr, "The Kolmogorov-Smirnov test for goodness of fit," *Journal of the American Statistical Association*, vol. 46, no. 253, pp. 68–78, 1951.

[8] L. J. Greenstein, D. G. Michelson, and V. Erceg, "Moment-method estimation of the Ricean $K$-factor," *IEEE Communications Letters*, vol. 3, no. 6, pp. 175–176, 1999.

[9] A. Abdi, C. Tepedelenlioglu, M. Kaveh, and G. Giannakis, "On the estimation of the $K$ parameter for the Rice fading distribution," *IEEE Communications Letters*, vol. 5, no. 3, pp. 92–94, 2001.